# Imaging Sub-Unit Cell Defects and Their Evolution in a Metal-Organic Framework

Lingmei Liu,[1,⊥] Zhijie Chen,[2,⊥] Jianjian Wang,[1,7,⊥] Daliang Zhang,[3,*] Yihan Zhu,[4] Sanliang Ling,[5] Kuo-wei Huang,[6] Youssef Belmabkhout,[2] Karim Adil,[2] Yuxin Zhang,[7] Ben Slater,[8,*] Mohamed Eddaoudi,[2,*] Yu Han[1,6,*]

[1] King Abdullah University of Science and Technology (KAUST), Physical Sciences and Engineering Division, Advanced Membranes and Porous Materials (AMPM) Center, Thuwal 23955-6900, Saudi Arabia
[2] KAUST, Physical Sciences and Engineering Division, AMPM Center, Functional Materials Design, Discovery and Development Research Group (FMD$^3$), Thuwal 23955-6900, Saudi Arabia
[3] KAUST, Core Labs, Thuwal, 23955-6900, Saudi Arabia
[4] Department of Chemical Engineering, Zhejiang University of Technology, Hangzhou 310014, P.R. China
[5] Advanced Materials Research Group, Faculty of Engineering, University of Nottingham, University Park, Nottingham NG7 2RD, United Kingdom
[6] KAUST, KAUST Catalysis Center (KCC), Thuwal 23955-6900, Saudi Arabia
[7] Multi-scale Porous Materials Center, Institute of Advanced Interdisciplinary Studies & College of Materials Science and Engineering, Chongqing University, Chongqing 400044, P. R. China
[8] Department of Chemistry, University College London, 20 Gordon Street, London WC1H 0AJ, United Kingdom

[⊥] These authors contributed equally to this work.

*Corresponding author. Email: daliang.zhang@kaust.edu.sa; b.slater@ucl.ac.uk; mohamed.eddaoudi@kaust.edu.sa; yu.han@kaust.edu.sa

**Defect engineering of metal–organic frameworks (MOFs) offers promising opportunities for tailoring their properties to specific functions and applications. However, determining the structures of defects in MOFs — either point defects or extended ones — has proved challenging owing to the difficulty of directly probing local structures in these typically fragile crystals. Here we report the real-space observation, with sub-unit-cell resolution, of structural defects in the catalytic MOF UiO-66 using a combination of low-dose transmission electron microscopy and electron crystallography. Ordered "missing linker" and "missing cluster" defects were found to co-exist. The missing-linker defects, reconstructed three-dimensionally with high precision, were attributed to terminating formate groups. The crystallization of the MOF was found to undergo an Ostwald ripening process, during which the defects also evolve: on prolonged crystallization, only the missing-linker defects remained. These observations were rationalised through density functional theory calculations. Finally,**

**the missing-cluster defects were shown to be more catalytically active than their missing-linker counterparts for the isomerization of glucose to fructose.**

MOFs are crystalline, porous materials, consisting of metal clusters (nodes) and organic coordinating ligands (linkers)[1-8]. In addition to manipulating the periodic bulk structure, defect tuning in MOFs has attracted considerable research attention, because it offers a means to locally tune porosity, create open-metal sites, and modulate surface properties, having important implications for separation, storage, catalysis, charge transport and mechanical responses[9-15]. UiO-66 is one of the most widely studied MOFs, largely due to its exceptional chemical stability[16] and catalytic activity that is linked to the presence of structural defects[15]. UiO-66 consists of hexanuclear clusters, six-centered metal (Zr, Hf or U) oxyhydroxide, each connected to 12 benzene-1,4-dicarboxylate (BDC) linkers (12-connected nodes; **fcu** net) with the nominal chemical formula $[M_6O_4(OH)_4][C_6H_4(COO)_2]_6$ (Fig. 1a)[16-18]. "Missing linker" and "missing cluster" defects, which respectively refer to the omission of a number of linkers and nodes from the perfect crystallographic structure, have been inferred to exist in UiO-66, but the exact structures of these defects and their spatial distribution remain ambiguous[19-24].

Non-stoichiometric compositions and unusual gas sorption behaviors are often used to affirm the presence of defects in UiO-66[19-21]. However, these proxies do not provide the atomic detail of the defect structures. Neutron powder diffraction[22] and synchrotron single-crystal X-ray diffraction[23,24] showed that a seemingly perfect UiO-66(Zr) contains ~10% of missing linkers. A combination of X-ray diffraction, electron diffraction and anomalous X-ray scattering identified the ordering of missing-cluster defects into nanoregions in a UiO-66(Hf) sample[25]. Fluorescence lifetime imaging revealed the spatial distribution of defects within individual UiO-67 (an isoreticular MOF of UiO-66) crystals at sub-micrometer resolution[26]. It is also known that the concentration of defects in UiO-66 can be tuned by adding various terminal monocarboxylic acids in the synthetic system as modulators[19]. However, despite numerous investigations of structural defects in UiO-66, many questions remain: What are the exact structures of the defects? Do the missing-linker defects form locally ordered domains as has been suggested for the missing-cluster defects[25]? Are there missing-linker defects and missing-cluster defects

coexisting in the same UiO-66 crystal? Can defect transformation occur during crystallization? All of these questions cannot be answered without a technique permitting to directly probe such defects.

High-resolution transmission electron microscopy (HRTEM) is a powerful tool to directly observe individual defects in real space, at atomic resolution[27]. However, conventional HRTEM is unsuitable for studying MOFs because the electron beam can easily damage their structures. High-angle annular dark-field scanning TEM has been used to observe metal clusters[28-31] and lattice distortion[28] in MOFs, but it did not disclose more structural details due to the limited resolution and weak contrast of organic components. Here, we combine our recently developed low-dose HRTEM technique[32,33] with electron crystallography to investigate defects in MOFs by real-space direct imaging. Our observations provide rich information about the defects in UiO-66, including their types, distributions and correlations, their exact three-dimensional (3D) structures, as well as their evolution.

**Results and discussion**

**Observation and 3D reconstruction of missing-linker defects.** A defective UiO-66 sample (denoted as UiO-66-D) was synthesized using formic acid (50 molar equivalents relative to BDC) as a modulator to promote the formation of defects. The powder X-ray diffraction (PXRD) pattern of UiO-66-D exhibits two broad, weak yet discernible peaks at 2θ of ~4° and ~6° (Fig. 1b), which are considered indicative of the presence of ordered missing-cluster nanoregions[25]. Analysis of the $N_2$ adsorption isotherm shows that UiO-66-D has a marked pore size distribution centered at 1.7 nm, in addition to the primary pores associated with the crystallographic structure (Fig. 1c). For comparison purposes, a nearly defect-free UiO-66 sample (UiO-66-P) is prepared and characterized; it does not show diffuse scattering features in the PXRD or extra pores of 1.7 nm (Fig. 1). These comparative results validate the reliability of the measurements, confirming that UiO-66-D encompasses a larger number of structural defects.

The HRTEM images presented in Figs. 2 and 3 were acquired from different areas of UiO-66-D consisting of interconnected irregular small (< 50 nm) particles. Their contrasts were

processed to be more directly interpretable by correcting the effect of the contrast transfer function (CTF) of the objective lens. Raw HRTEM images and low-magnification TEM images can be found in Supplementary Figs. 1 and 2, respectively. Images shown in Figs. 2a and 2b match the projected structural models and simulated potential maps of the perfect UiO-66(Zr) structure (*Fm*-3*m*; *a* = 20.7 Å) along the [001] and [110] directions, respectively. Interestingly, Fig. 2d has the same projection direction as Fig. 2b, but shows different image contrasts with apparent features of "missing linker": the contrasts of the horizontally arranged BDC ligands observed in Fig. 2b are not present in Fig. 2d (indicated by red arrows). As a consequence, adjacent opposing triangle-shaped channels in Fig. 2b are vertically merged into rhombus-shaped channels in Fig. 2d. A similar phenomenon is observed for the [001] images: the contrasts of benzene rings in the BDC ligands that are encompassed by four $Zr_6O_8$ clusters are clearly observed in Fig. 2a but not in Fig. 2c. These results indicate that, besides "perfect" regions (Figs. 2a-b), UiO-66-D has ordered regions consisting of missing-linker defects (Figs. 2c-e). In fact, the perfect structure is a minor component in UiO-66-D while most areas are defective with "missing linker" features, according to our HRTEM observations. The image in Fig. 2e shows a square arrangement of $Zr_6O_8$ clusters but a low plane symmetry of *p*2*mm*, suggesting that missing-linker defects give rise to a decrease in symmetry along one of the originally equivalent <001> directions.

By combining the HRTEM images from three distinct projections (Figs. 2c-e), the unit cell of the missing-linker region is determined as tetragonal with $a_{ML} = a/\sqrt{2}$ and $c_{ML} = a$, where *a* is the unit cell parameter of the parent UiO-66. The three images are thus indexed to the [001], [100], and [110] zone axis, respectively, according to the tetragonal crystal system. The observed reflection conditions ($h+k+l$ = 2n) from Fourier transforms (FTs) of the HRTEM images indicate an I-centered lattice (see Supplementary Fig. 3). Given that the [001], [100], and [110] images have projected symmetries of *p*4*mm*, *c*2*mm*, and *p*2*mm*, respectively, two space groups, *I*4/*mmm* (no. 139) and *I*422 (no. 97), are possible. We reconstructed the missing-linker defect by the electron crystallography technique, which renders a 3D electrostatic potential map from the Fourier summation of the crystal structure factors determined from the HRTEM images[34,35]. The reconstruction using space group of *I*4/*mmm* or *I*422 gave similar results (see

Supplementary Fig. 4). The reconstructed potential map clearly shows that the $Zr_6O_8$ clusters retain the same geometry as in the parent UiO-66; however, each cluster becomes 8-connected rather than 12-connected with neighboring clusters, converting the unit cell from a face-center cubic to a body-centered tetragonal structure (Fig. 2f). The resulting framework follows the underlying topology of a **bcu** net. The high precision of the reconstruction allows us to identify not only the $Zr_6O_8$ clusters and BDC ligands, but also the charge-compensating terminal formate ligands that substitute the missing bridging ligands to cap the open metal sites (Fig. 2f & Supplementary Fig. 5). The missing-linker defect can therefore be described as the result of the removal of all face-on BDC ligands from the parent UiO-66 structure, when it is projected along one of the <001> zone axes (Figs. 2a, c). The simulated 2-D projected potential maps of this structure perfectly match the HRTEM images, in all directions (Figs. 2c-e), which attests that the structure of the missing-linker defect has been correctly solved. We note that there is inconsistency in the literature with regard to defect termination in UiO-66: many papers argue for termination by monocarboxylates (i.e., formates when using formic acids as modulators),[19,36,37] whereas one study concluded that the defective sites are capped by water molecules and charge-balanced by hydroxides.[24] We employed liquid chromatography, $^{13}C$ NMR spectroscopy, and mass spectrometry to analyze HF-dissolved or thermally decomposed UiO-66-D samples (Supplementary Fig. 6). Our results provide substantive evidence that formates are present in this material (~ 4 wt%), corroborating the structural model we reconstructed from HRTEM.

**Identification of two types of "missing cluster" defects.** The missing-linker defect has the same extinction as the parent UiO-66 structure (Supplementary Fig. 7), and therefore does not account for the observed diffuse scattering in the PXRD. Cliffe *et al*. have correlated the diffuse peaks in the PXRD with short-range ordered missing-cluster defects, but evidence from HRTEM imaging could not be obtained due to beam damage[25]. In our HRTEM study, we occasionally observed, in different incidences, weak superlattice reflections that correspond to the extinct 100 and 110 reflections of pristine UiO-66, in agreement with the diffuse peaks in the PXRD; and we identified, in certain areas, nano-sized domains having ordered cluster vacancies, from which the superlattice reflections originate (Supplementary Fig. 8). These observations directly

correlate superlattice reflections with the missing-cluster defects. The observed missing-cluster domains are always only a few unit cells in dimension, much smaller than the missing-linker domains.

Fig. 3 shows typical [001] images containing missing-cluster domains. We note that the image contrast around the "missing cluster" differs between different domains. Fig. 3a and 3b represent two scenarios: the face-on BDC linkers, which are surrounding but not connected to the missing cluster, are present and absent, respectively. The first scenario is in good agreement with the missing-cluster model proposed by Cliffe *et al.*[25] that follows the underlying topology of an 8-connected **reo** net (Fig. 4). The second scenario, however, cannot be explained by the **reo** model, suggesting the coexistence of a different type of missing-cluster defect. The image contrast observed in Fig. 3b allows us to directly deduce a structural model that follows the underlying topology of an **scu** net, having one third of the $Zr_6O_8$ clusters 8-connected with surrounding clusters through BDC linkers, and the other two third 4-connected (Fig. 4). This **scu** model is validated by the HRTEM images of other directions containing missing-cluster defects (see Supplementary Figs. 8 and 9). The **reo** structure is realised by removing 1 out of 4 symmetry-equivalent $Zr_6O_8$ clusters along with the associated BDC linkers from each unit cell of the ideal UiO-66, while the **scu** model can be considered as removing clusters in a similar way, but from the **bcu** "missing linker" structure (Fig. 4). Therefore, the **scu** model has the same arrangement of clusters but it is more deficient in linkers, compared to the **reo** model.

We note that because the **scu** structure has similar projections as the **reo** structure in some orientations (see Supplementary Fig. 10), it is not always possible to distinguish them in HRTEM, although the missing clusters can be easily identified from the image contrast. Besides, the image contrast could be smeared and difficult to interpret if there are multiple structures and/or different orientations overlapping along the projection direction. In our study, this issue is largely avoided by choosing ultrafine crystallites (~ 20 nm) for imaging. In addition to well-defined **reo** and **scu** missing-cluster defects, we also observed large cavities in the UiO-66-D crystals resulting from irregular, continuous cluster vacancies (Supplementary Fig. 11). These results indicate the inhomogeneity in the local structure of this material.

**Relative stabilities of different defects.** We performed detailed density functional theory (DFT) calculations to infer the formation energies of missing-linker and missing-cluster defects from a comparison of the **bcu**, **reo** and **scu** structures with respect to the perfect **fcu** structure. We find that the relative stability follows the order of **fcu** > **bcu** > **reo** > **scu** and that the absolute defect formation energies for missing-linker and missing-cluster defects are reasonably small, consistent with the fact defects can be readily located by HRTEM, implying that they have a significant concentration (see additional discussions in Supplementary Table 1). The order of stability correlates with the connectivity in general. **fcu** is most stable due to its fully 12 connected network. The absolute defect formation energies of **bcu** and **reo** are similar, +17.8 and +20.4 kJ/mol per 3 $Zr^{4+}$ respectively, which is expected since their connectivity and stoichiometry is identical (8-connected net); **reo** is less stable because it contains missing clusters leading to a lower density (including larger voids and higher surface area (Supplementary Table 2)) than **bcu**. There is a modest enthalpic penalty increase for forming **scu** from **bcu** (+14.6 kJ/mol) *or* **reo** (+12.0 kJ/mol) as the connectivity of **scu** is lower (4, 8-connected net). Because the energy of forming any of the **bcu**, **reo** and **scu** structures from the perfect **fcu** material is relatively small, the calculations hint that all these defective structures are accessible under synthesis conditions. The accessible porosities of the four observed phases have been calculated based on the identified crystal structures, and the results indicate that both surface area and pore volume increase with the framework becoming more open, following the order of **fcu** < **bcu** < **reo** < **scu** (Supplementary Table 2).

**Defects evolution and crystals ripening.** The coexistence and comparable formation energies of "missing linker" and "missing cluster" defects in UiO-66 inspired us to investigate whether one could transform to the other. To this end, we synthesized UiO-66-D samples with varied crystallization time. We find that the diffuse scattering peaks in PXRD become apparently weaker when the crystallization time is increased from 1 day to 3 days; concurrently, the surface area and porosity of the product decrease, as determined from the $N_2$ sorption isotherms. In contrast, when the crystallization time was shortened to 1 hour, stronger diffuse scattering peaks and increased surface area and porosity are observed (Supplementary Fig. 12). These results indicate that the missing-cluster defects gradually disappear with prolonged

crystallization. Meanwhile, we note that the crystallization of UiO-66 is almost complete with a high product yield of 84% in 1 day; further extending crystallization time to 3 days leads to little change of product yields (88%) but significant increase in the crystal size from < 50 nm to ~100 nm (Supplementary Fig. 2). A direct conclusion from these observations is that UiO-66 crystals undergo a dissolution-redeposition (Ostwald ripening) process that is accompanied by the evolution of structural defects. Characterization of the 3-day sample with HRTEM confirms the fading of missing-cluster domains and reveals that ordered missing-linker defects remain predominant (Supplementary Fig. 13). On the other hand, the sample collected at 1 hour of crystallization (product yield: 48%) has both types of defects but a higher proportion of missing clusters compared to the 1-day sample (Supplementary Figs. 12-13). Taken together, we discovered a simultaneous evolution of crystal size and defective structure of UiO-66. Interestingly, we find that the defect evolution in UiO-66 is strongly dependent on the amount of the modulator, formic acid; for instance, when 175 molar equivalents of formic acid relative to BDC is used in the synthesis[25], the PXRD shows a *reverse* trend; missing-cluster defects are rapidly developed and grow in population as the crystallization time increases (Supplementary Fig. 14). The DFT assessment shows that in the absence of kinetic considerations, **fcu** is expected to be the thermodynamic product. However, the relatively low formation energy of the **bcu**, **reo** and **scu** structures suggest these structures could be accessible and are in fact evidenced directly through imaging here by HRTEM. The dilution of the BDC linker by modulating formic acid is critical in controlling the crystallisation behaviour; at low ratios of formic acid to BDC, the structure tends from defective towards perfect structure (**scu→bcu→fcu** or **scu→reo→fcu**), presumably driven by the exothermic changes to cohesive energy, and conversely under high ratios of formic acid to BDC, UiO-66 grows increasing populations of missing-cluster defects (**scu** or **reo**).

Unlike ordered missing-cluster defects that lead to additional PXRD peaks, ordered missing-linker defects are indistinguishable from the perfect structure by PXRD (Supplementary Fig. 7) but can be identified by HRTEM. In fact, we observed ordered missing-linkers in the 3-day UiO-66-D sample that would be considered nearly defect-free based on the PXRD *and* $N_2$ adsorption data, as well as in UiO-66-P that was prepared with acetic acid as modulator (Supplementary

Figs. 12-13). These results suggest that ordered missing-linker defects exist universally in various UiO-66 samples including those deemed seemingly perfect.

**Fine tuning the defects and catalytic activities of UiO-66.** The catalytic activity of UiO-66 has been correlated with the concentration of defects.[38,39] However, previous studies could not specify or distinguish the effects from "missing linker" defects and "missing cluster" defects.[38-41] In our study, the one-day and three-day UiO-66-D samples (hereafter respectively denoted as UiO-66-D(1d) and UiO-66-D(3d)) offer an opportunity to investigate the structure-activity relationships of this catalyst more definitively, because these samples have similar overall defect concentrations as indicated by the content of the defect-terminating formates (3.93 wt% and 3.65 wt%; Fig. 5a), while, at that same time, they have different concentrations of each type of defect: UiO-66-D(1d) has substantial amounts of both types of defects, whereas UiO-66-D(3d) is deficient in missing-cluster defects and dominated by missing-linker defects. We used the model reaction of the isomerization of glucose to fructose to evaluate catalytic activities during which the defects (under-coordinated $Zr^{4+}$) act as the catalytically active Lewis acid sites. As shown in Fig. 5b, UiO-66-D(1d) yielded markedly higher glucose conversion (47%) compared with UiO-66-D(3d) (34%) under identical reaction conditions, indicating that the catalytic sites in the configuration of "missing clusters" are more active than those in "missing linkers". We attribute this result to the possibility that the larger cavities associated with missing-cluster defects enhance the accessibility of the active sites.

By using a post-synthesis ligand-exchange method,[37] we could gradually "heal" the missing-linker defects to further tune the catalytic activity. Specifically, we prepared two samples by incubating UiO-66-D(3d) in BDC solution at 80 °C to facilitate ligand exchange (replacing formates with terephthalates). One sample (UiO-66-D(3d)-H1) experienced this healing process one time, while the other sample (UiO-66-D(3d)-H2) experienced it two times. The conditions of the healing process were carefully selected to ensure that ligand exchange rather than crystal dissolution and recrystallization took place, as indicated by the unaltered crystal sizes and morphologies of the healed samples (Supplementary Fig. 15). In comparison with UiO-66-D(3d), the healed samples had substantially fewer formates and smaller BET surface areas (Fig. 5a)

and their structures were predominantly “perfect” according to HRTEM (Supplementary Fig. 15), which attested to the success of the defect-healing process. When these materials were used as catalysts for glucose isomerization, their activities were in the following order: UiO-66-D(3d) > UiO-66-D(3d)-H1 > UiO-66-D(3d)-H2 (Fig. 5b), in accordance with the observed concentration of defects. These results demonstrate that our ability to tune and identify defects enables exploring the distinct roles of missing-linker and missing-cluster defects in the catalytic activity.

**Conclusion**

We directly imaged local structural defects in MOF UiO-66 by HRTEM. Unlike previous studies based on diffraction techniques which probe spatially averaged defect structures, our study reveals the coexistence of missing-linker and missing-cluster defects in the same crystal and their local structural ordering at atomic-scale. The high quality of our images enables a 3D reconstruction of the missing-linker defect, in which all the structural components including defect-terminating formate ligands, are clearly resolved. Two type of missing-cluster defects are also determined based on HRTEM. We discover that in the investigated system, missing-linker defects prevail, whereas missing-cluster defects only appear in small regions of few unit cell dimensions; and that with prolonged crystallization, missing-cluster defects vanish and missing-linker defects remain, along with the ripening of crystals. We also found that the trend of defect evolution can be reversed by increasing the concentration of modulator. We demonstrate that missing-cluster defects are catalytically more active than missing-linker defects at comparable defect concentrations. We use a post-synthesis ligand-exchange method to heal missing-linker defects and thus fine tuning of the catalytic activity for UiO-66.

We also see missing-linker defects in various UiO-66 samples including those that would be assumed to be essentially defect-free, which underlines that notionally perfect materials can contain defects invisible to most characterization techniques that may influence observed variance in properties of MOFs such as gas uptake[42,43]. The advent of low-dose HRTEM heralds a new way to explore the link between the functionality of MOFs and their activity through unambiguous structure determination. The methods we adopt in this work will also facilitate

the application of HRTEM to the investigation of local structures in other electron beam sensitive emerging functional materials such as COFs or porous cage materials[44].

## Data availability

The authors declare that all the data supporting the findings of this study are available within the paper and the Supplementary Information, and/or from the authors upon reasonable request.


## Acknowledgements

This research was supported by competitive center funds (FCC/1/1972-19) to Y.H. and M.E. from King Abdullah University of Science and Technology. This research used resources of the Core Labs of King Abdullah University of Science and Technology. Y.Z. acknowledges financial support from National Natural Science Foundation of China (21771161) and the Thousand Talents Program for Distinguished Young Scholars. S.L. and B.S. are thankful to the Materials Chemistry Consortium (EPSRC: EP/L000202) for provision of computer time on ARCHER UK National Supercomputing Service. B.S. wishes to acknowledge the Royal Society for financial support through an industry fellowship (F160062). The authors acknowledge helpful discussions with Andrew Goodwin, Matt Cliffe and Greig Shearer.


## Author contributions

Y.H., D.Z., and M.E. conceived and designed the experiments. L.L. acquired the low-dose high-resolution HRTEM images. Z.C., J.W., Y. B. and K. A. designed and synthesized MOF samples. Z.C., J.W. and Y.B. performed X-ray diffraction and $N_2$ adsorption characterizations. L.L., D.Z., Y.Z. and Y.H. processed and analyzed the HRTEM images. D.Z. solved the 3D structure of the missing linker defect. S.L. and B.S. performed theoretical calculations. J. W., Y.Z., and K.H. designed and performed the catalytic reactions. Y.H., D.Z., M.E., S.L. and B.S. wrote the manuscript and all authors commented on the manuscript.

## Competing interests

The authors declare no competing interests.

**Figure Captions**

**Figure 1 | Structural illustration and characterizations of UiO-66 samples. a**, (Left) crystallographic models of the perfect UiO-66 structure (atom colour code: Zr, cyan; O, red; C, grey; hydrogen atoms are omitted for clarity), and (Right) the corresponding topological representative. **b**, PXRD patterns of UiO-66-P and UiO-66-D. Black arrows indicate the broad diffuse scattering peaks. **c**, $N_2$ sorption isotherms and the derived pore size distribution profiles (inset) of the two materials. Compared to UiO-66-P, UiO-66-D has an extra pore size distribution centered at ~1.7 nm, which is not associated with the inter-particle porosity resulting in the significant adsorption at the high relative pressure region ($P/P_0 > 0.9$).

**Figure 2 | HRTEM analysis of perfect and "missing linker" regions in UiO-66-D. a-e,** CTF-corrected HRTEM images and structural models along the [001] (**a**) and [110] (**b**) zone axes of perfect UiO-66 (*Fm*-3*m*), and along the [001] (**c**), [100] (**d**) and [110] (**e**) zone axes of the missing linker defect (*I*4/*mmm*). In each panel, left, CTF-corrected image; middle, from the top-down are *p*1-averaged image, symmetry-imposed image, and simulated projected potential; right, the projected structural model. The similarity between the *p*1-averaged and symmetry-imposed images validates the symmetry determination. The similarity between the processed HRTEM image and the simulated projected potential in **c**, **d** and **e** validates the structural model of the missing linker defect. **f,** Reconstructed 3D electrostatic potential map viewed in different orientations with the structural model of the missing linker defect superimposed, showing an 8-connected network with the $Zr_6O_8$ clusters, BDC linkers and defect-terminating ligands (formates) that are all well resolved. In all structural models, the atom colour code is the same as described in Figure 1 with hydrogen atoms omitted for clarity. The scale bars represent 2 nm.

**Figure 3 | HRTEM analysis of the "missing cluster" defects in UiO-66-D.** CTF-corrected HRTEM images of the [001] direction, showing different types of missing-cluster defects: (**a**) **reo** and (**b**) **scu**. In the bottom panel of each figure, from left to right, are the projected structural model, the simulated projected potential map, and the experimental image (processed by real space

averaging to enhance the signal to noise ratio) for comparison. The unit cells used for averaging are labeled in the images with red dashed boxes. In the structural models, the atom colour code is the same as described in Figure 1. The scale bars represent 5 nm. The contrast associated with the BDC linkers surrounding the missing cluster is indicated by a red arrow in the simulated potential map in (**a**).

**Figure 4 |Illustrations of various defective structures in UiO-66.** (Top) crystallographic structural models and (Bottom) the corresponding topological representatives (2×2×2) of the 8-connected missing-linker defects (**bcu** net; transitivity [1112]), 8-connected missing-cluster defects (**reo** net; transitivity [1122]), and the 4,8-connected missing-cluster defects (**scu** net; transitivity [2133]). The transitivities [pqrs] denote p types of vertices, q types of edges, r types of faces and s types of tiles. Pink and yellow balls indicate 8- and 4-connected nodes, respectively. The atom colour code in the structural models is the same as described in Figure 1.

**Figure 5 |Characterization and catalytic performances of various defective UiO-66 samples. a,** Formate contents determined by high-performance liquid chromatography analysis of HF-digested solution (see the section of "Determination of the formate content in UiO-66 samples" in Supplementary Information for detailed method), and BET surface areas derived from $N_2$ sorption isotherms of four UiO-66 samples as labelled. **b,** Catalytic performances of various UiO-66 samples in the isomerization of glucose to fructose. "Blank" refers to the case without using a catalyst. The error bars represent standard uncertainties in the mean values calculated from five batches of repeated experiments. The dashed lines in (**b**) are used to guide eyes.

## References


1. Li, H., Eddaoudi, M., O'Keeffe, M. & Yaghi, O. M. Design and synthesis of an exceptionally stable and highly porous metal-organic framework. *Nature* **402,** 276-279 (1999).
2. Eddaoudi, M. *et al.* Systematic design of pore size and functionality in isoreticular MOFs and their application in methane storage. *Science* **295,** 469-472 (2002).
3. Yaghi, O. M. *et al.* Reticular synthesis and the design of new materials. *Nature* **423**, 705-714 (2003).
4. Horike, S., Shimomura, S. & Kitagawa, S. Soft porous crystals. *Nat. Chem.* **1,** 695-704 (2009).
5. Eddaoudi, M., Sava, D. F., Eubank, J. F., Adil, K. & Guillerm, V. Zeolite-like metal-organic frameworks (ZMOFs): design, synthesis, and properties. *Chem. Soc. Rev.* **44,** 228-249 (2015).
6. Li, J.-R., Kuppler, R. J. & Zhou, H.-C. Selective gas adsorption and separation in metal-organic frameworks. *Chem. Soc. Rev.* **38,** 1477-1504 (2009).
7. Férey, G. *et al.* A chromium terephthalate-based solid with unusually lLarge pore volumes and surface area. *Science* **309,** 2040-2042 (2005).
8. Chui, S. S.-Y., Lo, S. M.-F., Charmant, J. P. H., Orpen, A. G. & Williams, I. D. A Chemically functionalizable nanoporous material $[Cu_3(TMA)_2(H_2O)_3]_n$. *Science* **283,** 1148-1150 (1999).
9. Dissegna, S., Epp, K., Heinz, W. R., Kieslich, G. & Fischer, R. A. Defective metal-organic frameworks. *Adv. Mater*. **30,** 1704501 (2018).
10. Fang, Z., Bueken, B., De Vos, D. E. & Fischer, R. A. Defect-engineered metal–organic frameworks. *Angew. Chem. Int. Ed.* **54,** 7234-7254 (2015).
11. Bennett, T. D., Cheetham, A. K., Fuchs, A. H. & Coudert, F.-X. Interplay between defects, disorder and flexibility in metal-organic frameworks. *Nat. Chem.* **9,** 11-16 (2017).
12. Lee, J. *et al.* Metal-organic framework materials as catalysts. *Chem. Soc. Rev.* **38,** 1450-1459 (2009).
13. Sumida, K. *et al.* Carbon dioxide capture in metal–organic frameworks. *Chem. Rev.* **112,** 724-781 (2012).
14. Shoaee, M., Agger, J. R., Anderson, M. W. & Attfield, M. P. Crystal form, defects and growth of the metal organic framework HKUST-1 revealed by atomic force microscopy. *CrystEngComm* **10,** 646-648 (2008).
15. Ling, S. & Slater, B. Dynamic acidity in defective UiO-66. *Chem. Sci.* **7,** 4706-4712 (2016).
16. Cavka, J. H. *et al.* A new zirconium inorganic building brick forming metal organic frameworks with exceptional stability. *J. Am. Chem. Soc.* **130,** 13850-13851 (2008).
17. Jakobsen, S. *et al.* Structural determination of a highly stable metal-organic framework with possible application to interim radioactive waste scavenging: Hf-UiO-66. *Phys. Rev. B* **86,** 125429 (2012).
18. Falaise, C. *et al.* Three-dimensional MOF-type architectures with tetravalent uranium hexanuclear motifs ($U_6O_8$). *Chem. Eur. J.* **19,** 5324-5331 (2013).
19. Shearer, G. C. *et al.* Defect engineering: tuning the porosity and composition of the metal–organic framework UiO-66 via modulated mynthesis. *Chem. Mater.* **28,** 3749-3761 (2016).
20. Shearer, G. C. *et al.* Tuned to perfection: Ironing out the defects in metal–organic framework UiO-66. *Chem. Mater.* **26,** 4068-4071 (2014).
21. Valenzano, L. *et al.* Disclosing the complex structure of UiO-66 metal organic framework: A synergic combination of experiment and theory. *Chem. Mater.* **23,** 1700-1718 (2011).
22. Wu, H. *et al.* Unusual and highly tunable missing-linker defects in zirconium metal–organic framework UiO-66 and their important effects on gas adsorption. *J. Am. Chem. Soc.* **135,** 10525-10532 (2013).

23. Øien, S. *et al.* Detailed structure analysis of atomic positions and defects in zirconium metal–organic frameworks. *Cryst. Growth Des.* **14,** 5370-5372 (2014).
24. Trickett, C. A. *et al.* Definitive molecular level characterization of defects in UiO-66 crystals. *Angew. Chem. Int. Ed.* **54,** 11162-11167 (2015).
25. Cliffe, M. J. *et al.* Correlated defect nanoregions in a metal–organic framework. *Nat. Commun.* **5,** 4176 (2014).
26. Schrimpf, W. *et al.* Chemical diversity in a metal–organic framework revealed by fluorescence lifetime imaging. *Nat. Commun.* **9,** 1647 (2018).
27. Hashimoto, A., Suenaga, K., Gloter, A., Urita, K. & Iijima, S. Direct evidence for atomic defects in graphene layers. *Nature* **430,** 870-873 (2004).
28. Platero-Prats, A.E. *et al*. Bridging zirconia nodes within a metal-organic framework via catalytic Ni-hydroxo clusters to form heterobimetallic nanowires. *J. Am. Chem. Soc.* **139,** 10410-10418 (2017).
29. Mehdi, B.L. *et al*. Low-dose and In-Painting methods for (near) atomic resolution STEM imaging of metal organic frameworks (MOFs). *Microsc. Microanal.* **23,** 1804-1805 (2017).
30. Mayoral, A., Sanchez-Sanchez, M., Alfayate, A., Perez-Pariente, J. & Diaz, I. Atomic observations of microporous materials highly unstable under the electron beam: the cases of Ti-doped $AlPO_4$-5 and Zn-MOF-74. *ChemCatChem* **7,** 3719-3724 (2015).
31. Leus, K. *et al*. Atomic layer deposition of Pt nanoparticles within the cages of MIL-101: a mild and recyclable hydrogenation catalyst. *Nanomaterials* **6,** 45 (2016).
32. Zhu, Y. *et al.* Unravelling surface and interfacial structures of a metal–organic framework by transmission electron microscopy. *Nat. Mater.* **16,** 532-537 (2017).
33. Zhang, D. *et al.* Atomic-resolution transmission electron microscopy of electron beam–sensitive crystalline materials. *Science* **359,** 675–679 (2018).
34. Sakamoto, Y. *et al.* Direct imaging of the pores and cages of three-dimensional mesoporous materials. *Nature* **408,** 449-453 (2000).
35. Han, Y. *et al.* A tri-continuous mesoporous material with a silica pore wall following a hexagonal minimal surface. *Nat. Chem.* **1,** 123-127 (2009).
36. Vandichel, M. et al. Active site engineering in UiO-66 type metal-organic frameworks by intentional creation of defects: a theoretical rationalization. *CrystEngComm* **17,** 395-406 (2015).
37. Taddei, M., Wakeham, R.J., Koutsianos, A., Andreoli, E. & Barron, A.R. Post-synthetic ligand exchange in zirconium-based metal-organic frameworks: beware of the defects! *Angew. Chem. Int. Ed.* **57,** 11706-11710 (2018).
38. Vermoortele, F. *et al.* Synthesis modulation as a tool to increase the catalytic activity of Metal–Organic Frameworks: the unique case of UiO-66(Zr). *J. Am. Chem. Soc.* **135,** 11465-11468 (2013).
39. Korzyński, M. D., Consoli, D. F., Zhang, S., Román-Leshkov, Y. & Dincă, M. Activation of methyltrioxorhenium for olefin metathesis in a zirconium-based metal–organic framework. *J. Am. Chem. Soc.* **140,** 6956-6960 (2018).
40. Liu, Y., Klet, R.C., Hupp, J.T. & Farha, O. Probing the correlations between the defects in metal-organic frameworks and their catalytic activity by an epoxide ring-opening reaction. *Chem. Commun.* **52,** 7806-7809 (2016).
41. De Mello, M.D. & Tsapatsis, M. Selective glucose-to-fructose isomerization over modified zirconium UiO-66 in alcohol media. *ChemCatChem* **10,** 2417-2423 (2018).
42. Sholl, D. S. & Lively, R. P. Defects in metal–organic frameworks: challenge or opportunity? *J. Phys. Chem. Lett.* **6,** 3437-3444 (2015).
43. Park, J., Howe, J. D., & Sholl, D. S. How reproducible are isotherm measurements in metal–organic frameworks? *Chem. Mater.* **29,** 10487-10495 (2017).

44. Jones, J. T. A. *et al.* Modular and predictable assembly of porous organic molecular crystals. *Nature* **474,** 367-371 (2011).

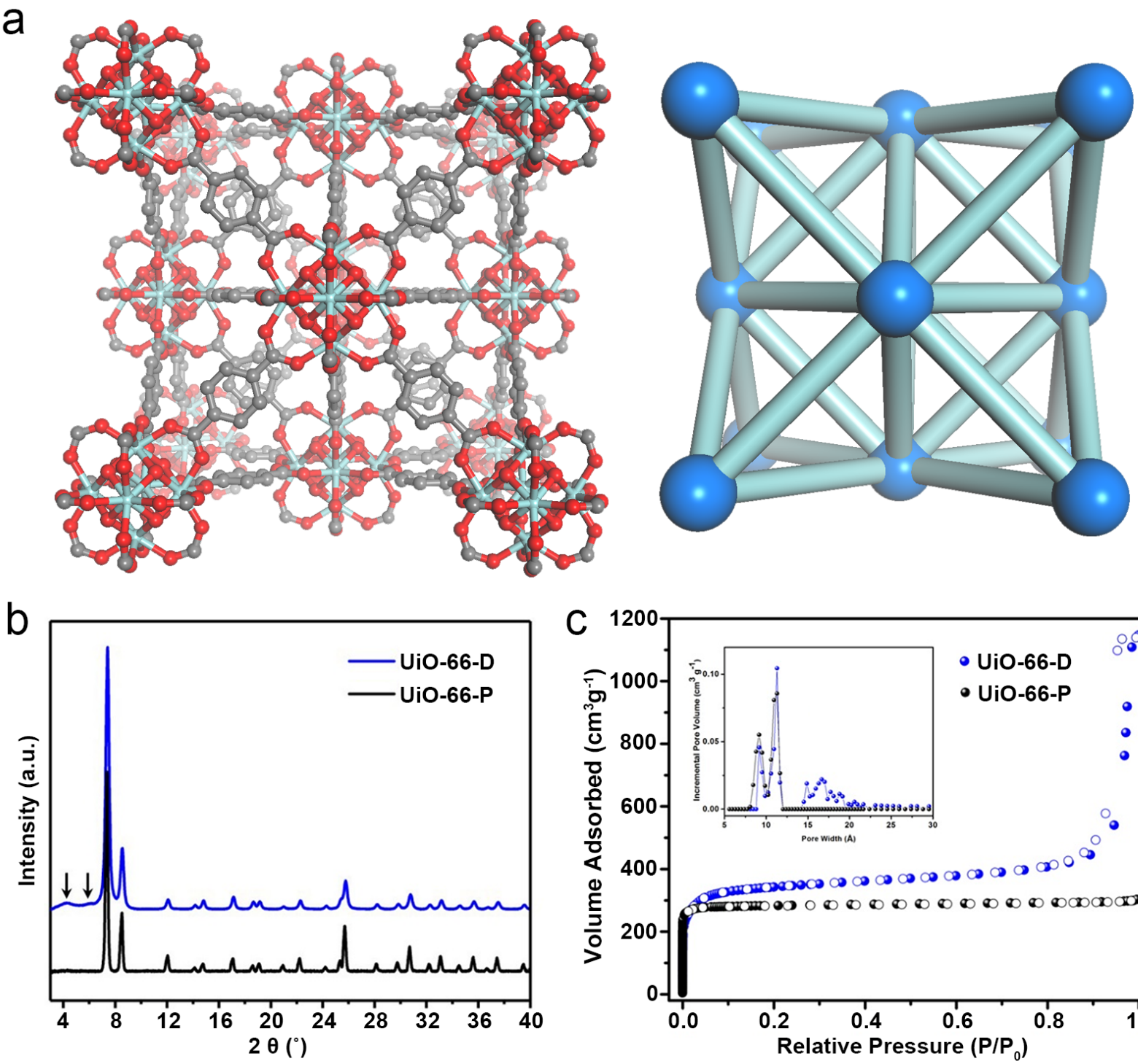
a
b
UiO-66-D
UiO-66-P
Intensity (a.u.)
2 θ (˚)
c
Volume Adsorbed (cm3g-1)
Relative Pressure (P/P0)
Incremental Pore Volume (cm3 g-1)
Pore Width (Å)

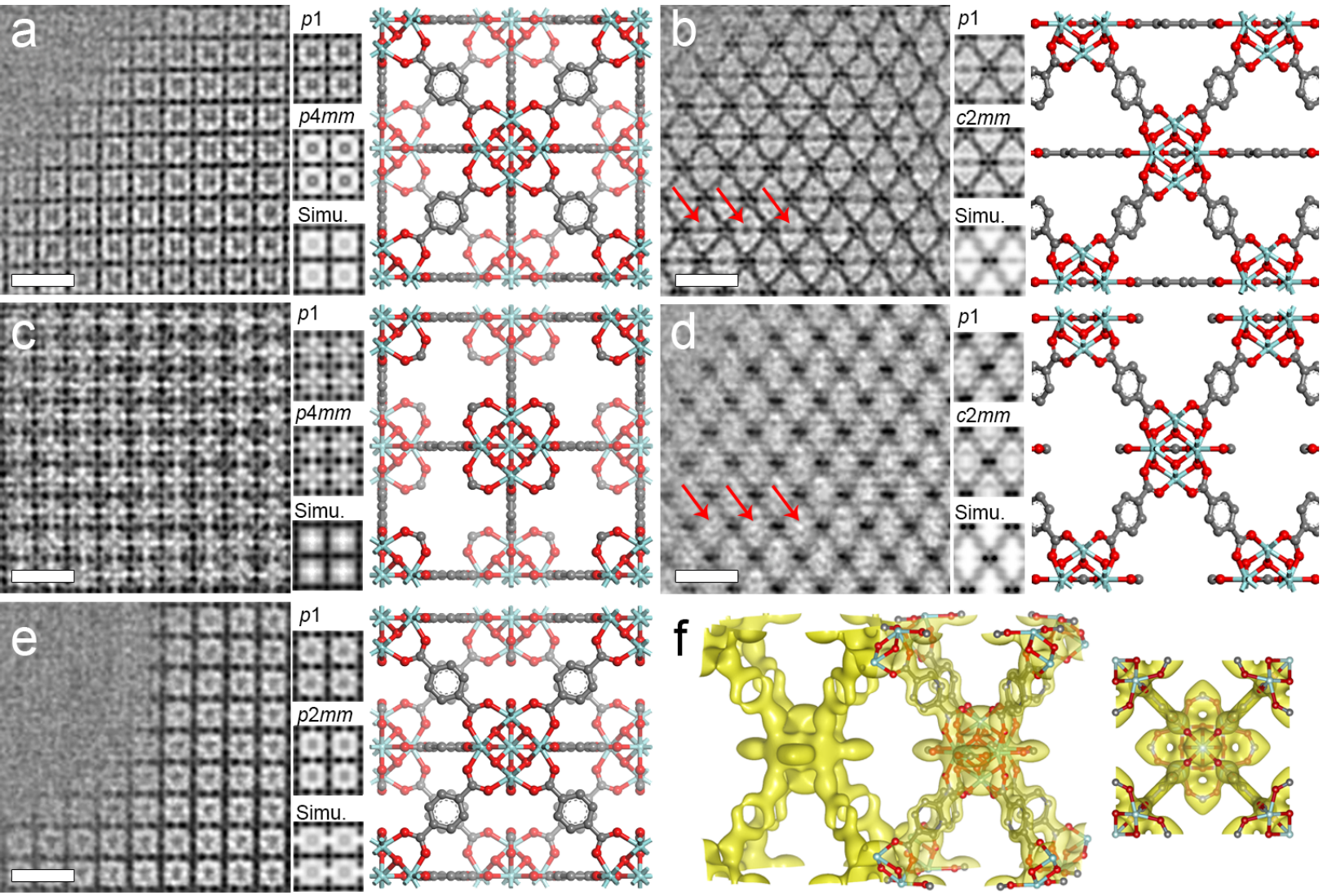
a
p1
p4mm
Simu.
b
p1
c2mm
Simu.
c
p1
p4mm
Simu.
d
p1
c2mm
Simu.
e
p1
p2mm
Simu.
f

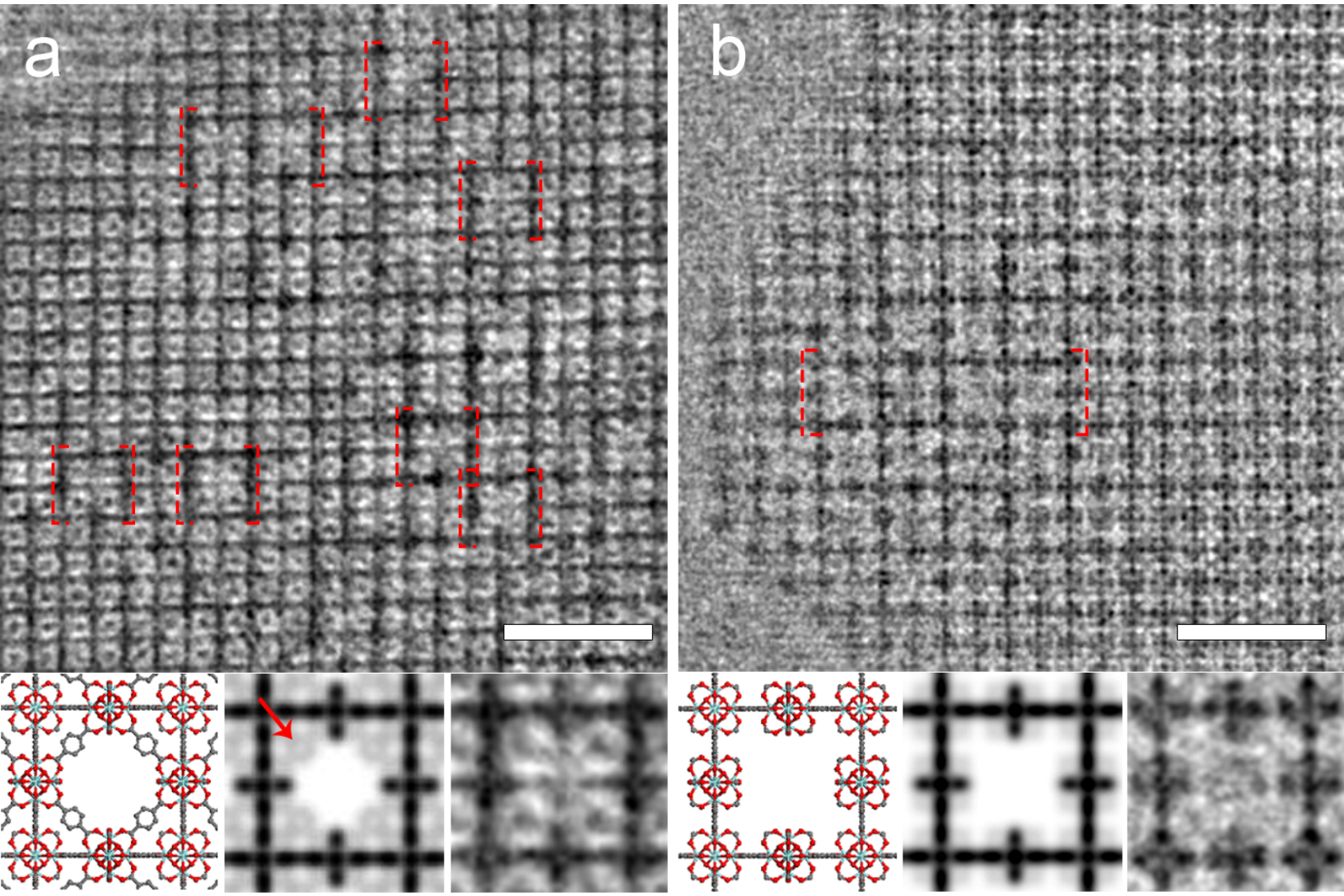
a
b

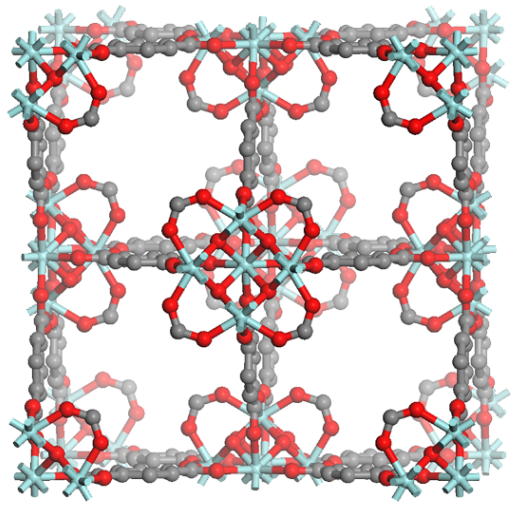

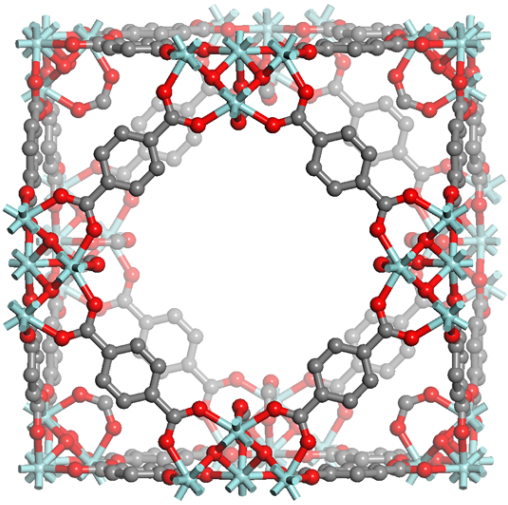

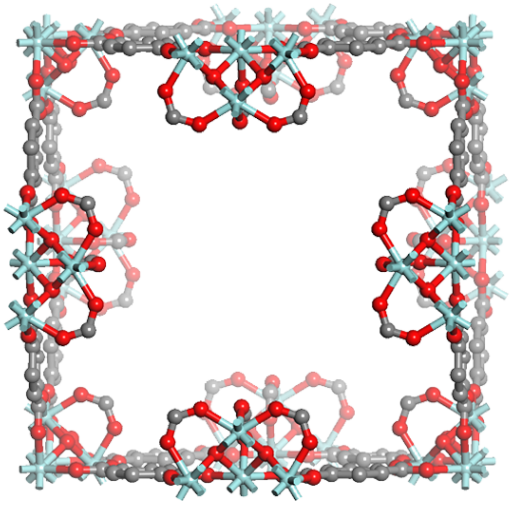

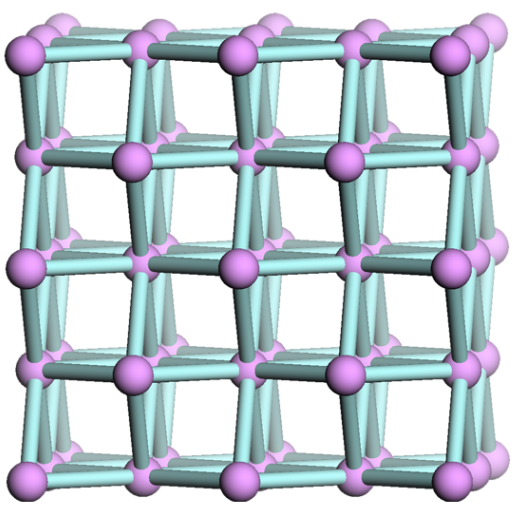

**bcu** 8-c net

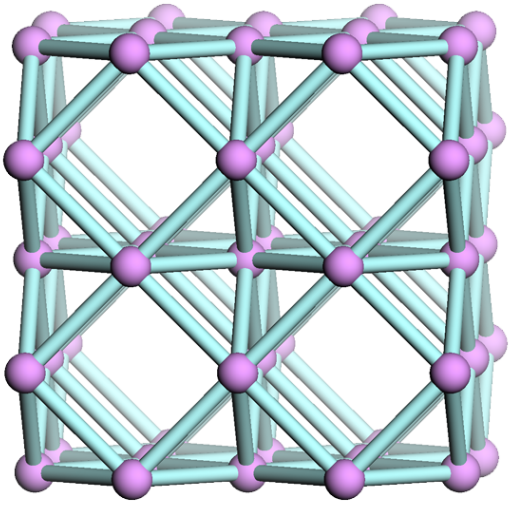

**reo** 8-c net

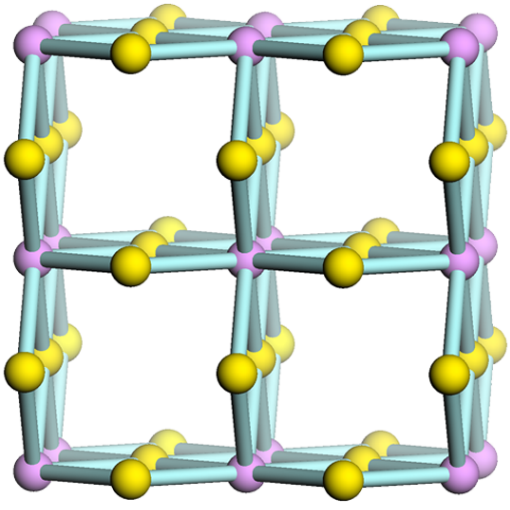

**scu** 4, 8-c net

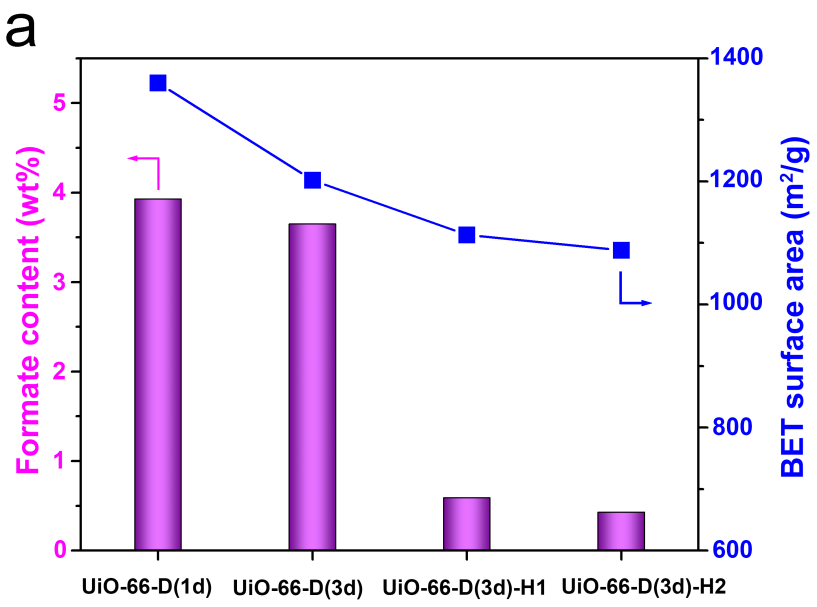
a
Formate content (wt%)
BET surface area (m²/g)
0
1
2
3
4
5
600
800
1000
1200
1400
UiO-66-D(1d)
UiO-66-D(3d)
UiO-66-D(3d)-H1
UiO-66-D(3d)-H2

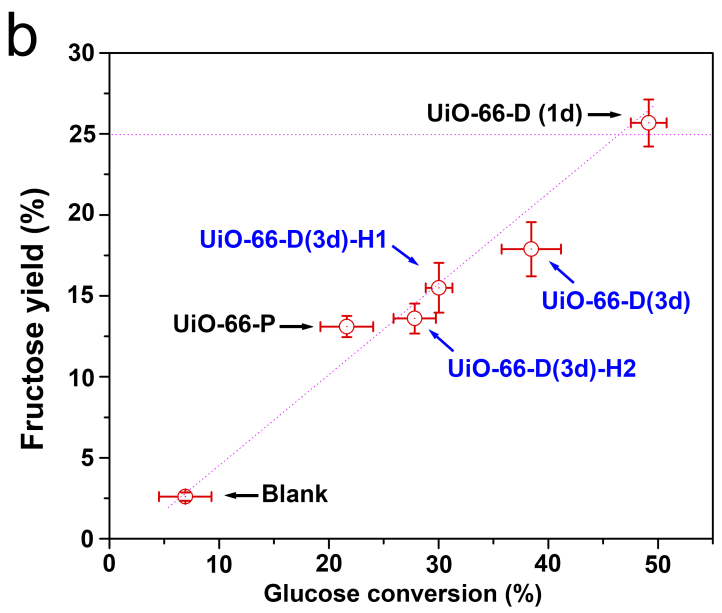
b
Fructose yield (%)
Glucose conversion (%)
0
5
10
15
20
25
30
0
10
20
30
40
50
UiO-66-D (1d)
UiO-66-D(3d)-H1
UiO-66-D(3d)
UiO-66-P
UiO-66-D(3d)-H2
Blank

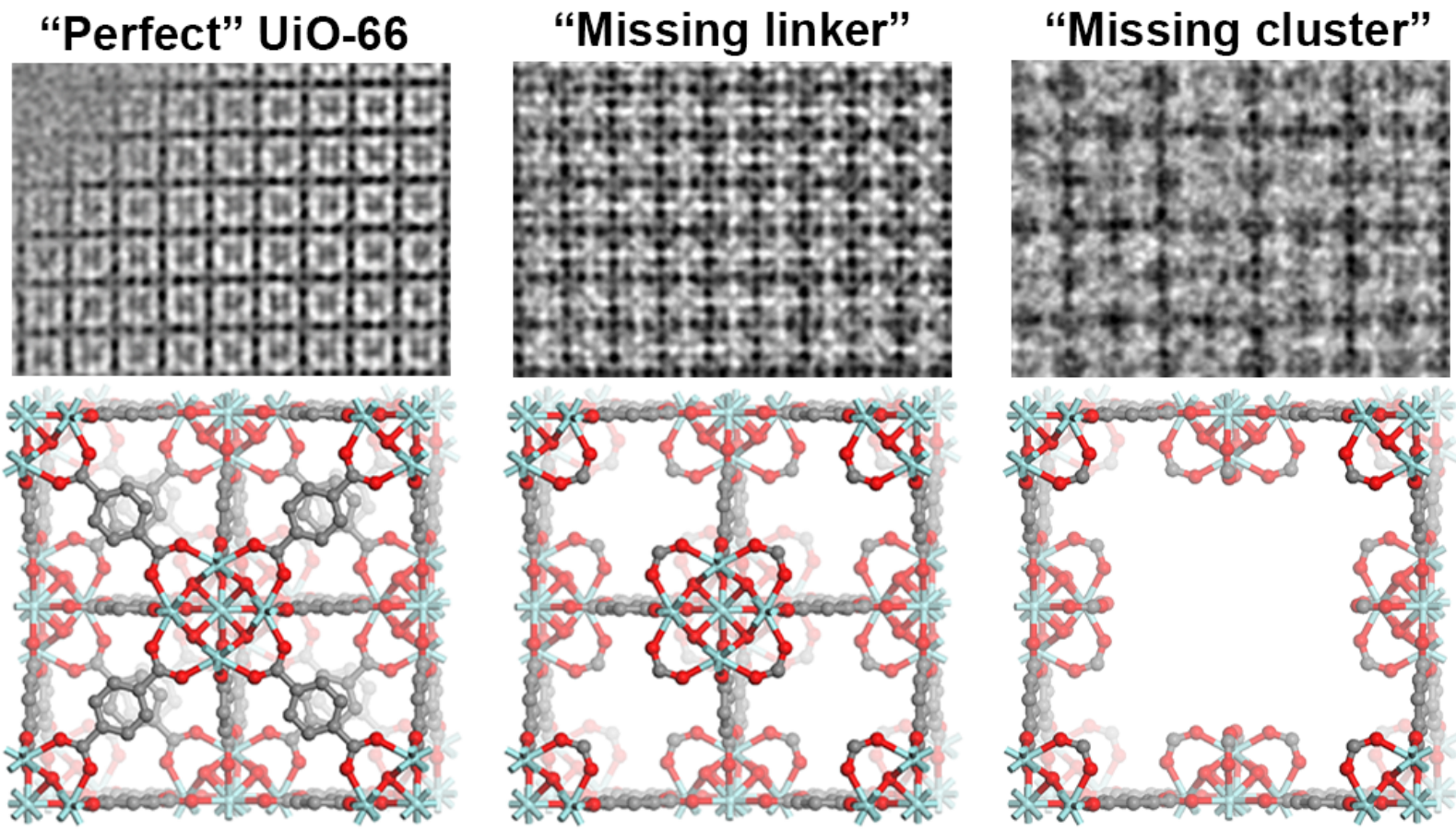
“Perfect” UiO-66
“Missing linker”
“Missing cluster”